

HHS Public Access

Author manuscript

IEEE Robot Autom Mag. Author manuscript; available in PMC 2020 May 01.

Published in final edited form as:

IEEE Robot Autom Mag. 2019 May; 2019: 9834–9840. doi:10.1109/ICRA.2019.8794245.

Steering a Multi-armed Robotic Sheath Using Eccentric Precurved Tubes

Jiaole Wang, Ha Junhyoung, Pierre E. Dupont

Department of Cardiovascular Surgery, Boston Children's Hospital, Harvard Medical School, Boston, MA 02115, USA.

Abstract

This paper presents a novel continuum robot sheath for use in single-port minimally invasive procedures such as neuroendoscopy in which the sheath is designed to deliver multiple robotic arms. Articulation of the sheath is achieved by using precurved superelastic tubes lining the working channels used for arm delivery. These tubes perform a similar role to push/pull tendons, but can accomplish shape change of the sheath via rotation as well as translation. A kinematic model using Cosserat rod theory is derived which is based on modeling the system as a set of eccentrically aligned precurved tubes constrained along their length by an elastic backbone. The specific case of a two-arm sheath is considered in detail and its relationship to a concentric tube balanced pair is described. Simulation and experiment are used to investigate the concept, map its workspace and to evaluate the kinematic model.

Keywords

Steerable sheath; Multiple arms; Concentric tube robots

I. Introduction

Compared to multi-port minimally invasive surgeries, single-port endoscopic procedures offer a number of advantages to the patient. These include reduced pain due to fewer incisions and hemorrhaging, and shorter recovery time [1], [2]. In neurosurgery, endoscopy enables navigation through the clear fluid-filled ventricular system of the brain instead of through healthy brain tissue enabling minimally invasive treatment of tumors [3]–[6], cysts [7]–[9], hydrocephalus [10], [11] and epileptogenic lesions [12]. Twenty percent of brain tumors lie either adjacent to, or inside, the ventricles, and endoscopy has had a major impact in their treatment leading to reductions in morbidity and procedure time [13], [14].

A major challenge is that many neuroendoscopes include a single working channel forcing clinicians to perform onehanded surgery. This approach requires substantial training, leads to longer procedure times and limits the types of procedures that can be performed. While some rigid endoscopes do allow simultaneous use of two tools, the tools are mounted on straight parallel shafts making it difficult to perform critical tasks like hemostasis. Furthermore, orienting the endoscope tip with respect to the lesion is also challenging and while manual flexible endoscopes provide some steerability, they provide a single working channel and their curvature can make tool control difficult.

A single-port robotic system as shown in Fig. 1 can address these challenges by providing two or more articulated arms deployed from a steerable endoscopic sheath. While a variety of systems of this type have been developed [15], the sheath diameter of these devices is too large for neurosurgery as well as for other types of procedures. The challenge of miniaturization is to provide sufficient cross section in the sheath for the arm working channels and optics while also enabling steerable control of the sheath.

Several continuum robot technologies are available to produce a steerable sheath. These include those that use tendons attached to the distal end of a central backbone to cause deflection by pulling [16]. Similarly, tubes can be used instead of tendons to enable both pulling and pushing [17]–[19]. A sheath could also be constructed as a concentric tube robot [20], [21]. Since the maximum curvature of concentric tube robots is inversely proportional to their overall diameter, however, tendon/tube designs provide higher curvatures as diameter increases. Nevertheless, reducing sheath diameter while preserving arm working channel diameters and also accommodating the stiffness of the arms passing through the sheath poses limits on what can be achieved.

While the arm working channels are typically viewed as passive lumens, this paper explores an alternative approach to sheath steering in which precurved superelastic tubes lining the working channels for the arms are used to produce sheath deflection. While actuation could include both rotating and translating these precurved tubes with respect to the sheath, the case of pure rotation is considered here. Since the arm diameters are typically at least a factor of two smaller than the sheath diameter, the maximum precurvature of these tubes is proportionally larger than what could be achieved with a sheath constructed from concentric tubes.

The contribution of this paper is to model and characterize the capabilities of this sheath design. The remainder of paper is organized as follows. Section II considers a sheath comprised of two arm channels. Section III develops a mechanics-based kinematic model for an arbitrary number of arms. The workspace and effect of parameters, such as the spacing between the arms, are demonstrated through simulation for the two-arm design in Section IV. These results are validated experimentally in Section V while conclusions appear in the final section.

II. Two-arm Sheath Design

Considering a pair of arm channels, a schematic of the proposed continuum robot sheath is shown in Fig. 2. The two pre-curved tubes lining the arm channels can be rotated at the proximal end with respect to the sheath and with respect to each other. As depicted, disks spaced along the length of the sheath are attached to a central backbone. These disks constrain the relative positions of the arm channel tubes. The role of the central backbone is solely to maintain the distance between the disks and so is assumed to be axially very stiff, but with arbitrary bending and torsional stiffness. This continuum mechanism is similar to the well-studied concentric tube balanced pair [22] except that the tubes are now offset from each other – forming what we will term an eccentric tube robot. Depending on the selected

bending and torsional stiffness of the central backbone, one can consider the overall structure to be comprised of three eccentrically arranged tubes.

We would like to select the pre-curvatures and relative stiffnesses of the two arm tubes so as to design a sheath that can deflect its tip in both the X and Y directions. It may also be necessary to rotate the arms about the Z axis to correctly position the arms with respect to the surgical site. Consequently, we are also interested in how rotation of the working channel tubes may result in twisting of the sheath.

In order to avoid a hole in the middle of the workspace, we consider the case here in which the pre-curvature and stiffness of the two tubes are equal – matching the design of a concentric tube balanced pair. The kinematic configuration of Fig. 2 shows the case in which the pre-curvatures of the two tubes are aligned. we can anticipate that as both tubes are simultaneously rotated, the tip of the sheath will roughly trace out a circle. The curvature will be slightly smaller in the depicted configuration compared to the case in which the tubes are aligned with the Y plane. This is because the tubes lie above and below the neutral axis in the depicted configuration while rotating both by 90° centers them both on the neutral axis.

To straighten the sheath, the two tubes must be rotated such that their curvatures cancel each other. Three potential configurations for achieving this are shown in Fig. 3. In the configurations of Fig. 3(a) and (b), the tubes are coplanar. In Fig. 3(c), they are offset from each other, producing a moment with respect to the central axis. while this configuration will likely result in a straight sheath which is twisted along its length.

For configurations consisting of rotations between the extreme cases of Figs. 2 and 3, we can anticipate that the sheath will take on an intermediate value of curvature and of twist. To determine the specific relationship between arm tube angles $\{a_1, a_2\}$ and sheath shape along with the dependency on model parameters (e.g., arm eccentricity, disk spacing), we derive the kinematic model below.

III. Kinematic Modeling

While a two-arm sheath design is described above, we consider here a sheath with an arbitrary number of arms. To derive the model, which bears similarity to those previously proposed for push/pull tendon tubes [23], [24], the following assumptions are made:

- Tubes and backbone are assumed flexible in bending and twisting, but axially rigid and experience no cross-sectional shear deformation.
- Disks are assumed rigid, perpendicular to the central backbone and the arm channels are equidistant from the backbone.
- Disks constrain centerline position of arm tubes, but not their orientation. (This allows twisting of the sheath.)
- No external loads are applied.
- Weights of disks, backbone and tubes are neglected.

A. Modeling Arm Tubes and Central Backbone Between Disks

The pre-curved tubes of each arm working channel together with central backbone can all be modeled as Cosserat rods that are cantilevered at their proximal ends and subject to forces and moments applied to each other through the disks. As shown in Fig. 4, a fixed global frame can be defined at the proximal end while the solid and dashed lines show the initial and the deformed shapes of the rod, respectively. Each rod is parameterized by the curve length s that s = 0 at the cantilevered end, and $s = \ell$ at the distal end. The variables $\mathbf{p}(s) \in \mathbb{R}^3$ and $\mathbf{R}(s) \in SO(3)$ are the position and orientation of the body local frame at s. A superscript of * is used to denote initial position and orientation.

The rods are subject to arbitrary external distributed forces $\mathbf{f}(s)$ and distributed moments $\mathbf{t}(s)$. The internal force $\mathbf{n}(s)$ and moment $\mathbf{m}(s)$ at the cross section of position $\mathbf{p}(s)$ are the resulting reaction force and moment from the external loads acting from s to ℓ Therefore, the force and moment equilibrium equations for the individual rods expressed in the global frame are as follows,

$$\int_{s}^{\ell} \mathbf{f}(\delta) \, d\delta - \mathbf{n}(s) = 0,\tag{1}$$

$$\int_{s}^{\ell} [\mathbf{p}(\delta) \times \mathbf{f}(\delta) + \mathbf{t}(\delta)] d\delta - \mathbf{m}(s) - \mathbf{p}(s) \times \mathbf{n}(s) = 0.$$
 (2)

By taking the derivatives of (1) and (2) with respect to s, we have

$$\dot{\mathbf{n}}(s) = -\mathbf{f}(s),\tag{3}$$

$$\dot{\mathbf{m}}(s) = -\dot{\mathbf{p}}(s) \times \mathbf{n}(s) - \mathbf{t}(s). \tag{4}$$

We can rewrite the moment equation in terms of curvature by introducing a constitutive equation. Assuming linear elastic behavior,

$$\mathbf{m}(s) = \mathbf{R}(s)\mathbf{K}(\mathbf{u}(s) - \mathbf{u}^*(s)) \tag{5}$$

in which $\mathbf{u}(s)$ and $\mathbf{u}^*(s)$ stand for the current and relaxed curvatures of the rod, respectively. The stiffness matrix $\mathbf{K} \in \mathbb{R}^{3\times 3}$ is a diagonal matrix as

$$\mathbf{K}(s) = \begin{bmatrix} K_b & 0 & 0 \\ 0 & K_b & 0 \\ 0 & 0 & K_t \end{bmatrix},$$

where $K_b = EI$ and $K_t = GJ$ are the bending and torsional stiffness of the tube, E and G are the Young's and shear moduli, and $G = \frac{E}{2(1+v)}$ where v stands for the Poisson's ratio. I and J are the second moment of area and polar moment of the inertial of the cross section, respectively.

Differentiating (5) and substituting into (4) yields a differential equation in curvature given by

$$\dot{\mathbf{u}} = \dot{\mathbf{u}}^* - \mathbf{K}^{-1} \left[\hat{\mathbf{u}} \mathbf{K} (\mathbf{u} - \mathbf{u}^*) + \hat{\mathbf{e}}_3 \mathbf{R}^\mathsf{T} \mathbf{n} + \mathbf{R}^\mathsf{T} \mathbf{t} \right]. \tag{6}$$

in which the $\hat{\cdot}$ operator maps SO(3) to so(3) as defined in [25].

Given the assumption of no external loads, the only forces and moments experienced by the rods are applied by the disks. With the assumption of zero disk thickness, the interaction between disks and tubes remains only the point forces. These will be treated as boundary conditions with integration carried out between each pair of disks, where there is no force interaction. Consequently, we can omit the distributed force and torque terms resulting in the following set of equations for arm tubes and central backbone.

$$\begin{cases} \dot{\mathbf{p}}_{j} = \mathbf{R}_{j} \mathbf{e}_{3}, \\ \dot{\mathbf{R}}_{j} = \mathbf{R}_{j} \hat{\mathbf{u}}_{j}, \\ \dot{\mathbf{u}}_{j} = \dot{\mathbf{u}}_{j}^{*} - \mathbf{K}_{j}^{-1} \left[\hat{\mathbf{u}}_{j} \mathbf{K}_{j} (\mathbf{u}_{j} - \mathbf{u}_{j}^{*}) + \hat{\mathbf{e}}_{3} \mathbf{R}_{j}^{\mathsf{T}} \mathbf{n}_{j} \right], \\ \dot{\mathbf{n}}_{j} = \mathbf{0}, \end{cases}$$

$$(7)$$

where the subscript $j \in [0, \dots, m]$ denotes the index for the arm tubes, and j = 0 stands for the backbone; $\mathbf{e}_3 = [0,0,1]^T$.

B. Compatibility Conditions Imposed by Disks

The disks constrain the relative position of the rods as shown in Fig. 5. A complication is that the arm tubes can slide with respect to the disks. Thus, each arm tube passes through a disk at a slightly different arc length than that of the central backbone. We introduce a sliding variable $s_{j,k}$ to capture this phenomenon. The disk compatibility conditions can then be written as

$$\mathbf{p}_{i}(s_{k} + \Delta s_{i,k}) = \mathbf{R}_{0}(s_{k})\mathbf{r}_{i,k}(s_{k}) + \mathbf{p}_{0}(s_{k}), \tag{8}$$

where $s_{j,k}$ and s_k are the curve lengths of the *j*-th tube at the *k*-th disk and curve length of the backbone at *k*-th disk, respectively. The Z-axis component of $\mathbf{r}_{j,k}(s_k)$ equals to 0 in the local disk frame as shown in Fig. 5.

C. Boundary Conditions

For both the arm tubes and central backbone, rod position and orientation are preserved at each disk:

$$\mathbf{p}_0(s_k^-) = \mathbf{p}_0(s_k^+), \quad \mathbf{R}_0(s_k^-) = \mathbf{R}_0(s_k^+),$$
 (9)

$$\mathbf{p}_{j}(s_{j,k}^{-}) = \mathbf{p}_{j}(s_{j,k}^{+}), \ \mathbf{R}_{j}(s_{j,k}^{-}) = \mathbf{R}_{j}(s_{j,k}^{+}), \ \mathbf{u}_{j}(s_{j,k}^{-}) = \mathbf{u}_{j}(s_{j,k}^{+}).$$
(10)

The superscripts – and + denote the values before and after the k-th disk. It is also assumed that at the proximal disk, $s = s_j = 0$, each arm tube is aligned with the central backbone along the Z axis.

Since the tubes interact with the disks at discrete points along their length, the interaction forces between the arm tubes and disks will be point forces as shown in Fig. 6. Under the frictionless assumption, the point force exerted by the *k*-th disk on the *j*-th tube should be perpendicular to the tube, $\mathbf{f}_{p_{j,k}} = \left[f_{jkx}, f_{jky}, 0 \right]^{\mathsf{T}}$.

The boundary conditions express the discontinuities in internal force and moment at each disk. For the arm tubes, the force equations can be written as

$$\mathbf{n}_{j}(s_{j,k}^{-}) = \mathbf{n}_{j}(s_{j,k}^{+}) + \left(\mathbf{R}_{j}\mathbf{f}_{p_{j,k}}\right), \tag{11}$$

$$s_{i,k} = s_k + \Delta s_{i,k}. \tag{12}$$

Recall that $s_{j,k}$ models the sliding of the arm tubes with respect to the disks and central backbone.

The arm tube forces applied to the disk will generate both forces and torques on the central backbone. The forces are the reacting forces $-\mathbf{f}_{pj,k}$ acting on the hole positions of backbone. Then the torques will be generated due to the offsets. Referring to Fig. 5, the resulting discontinuities in curvature and cross section force are given by

$$\mathbf{m}_{0}(s_{k}^{-}) = \mathbf{m}_{0}(s_{k}^{+}) + \mathbf{R}_{0} \sum_{j=1}^{g} \left[\mathbf{r}_{j,k} \times (-\mathbf{R}_{0}^{\mathsf{T}} \mathbf{R}_{j} \mathbf{f}_{p_{j,k}}) \right], \tag{13}$$

$$\mathbf{n}_{0}(s_{k}^{-}) = \mathbf{n}_{0}(s_{k}^{+}) + \left(-\sum_{j=1}^{m} \mathbf{R}_{j} \mathbf{f}_{p_{j,k}}\right). \tag{14}$$

In addition, at the distal disk, the net internal forces and moments for both the arm tubes and the backbone must be zero.

D. Solution Approach

The interactive forces $\mathbf{f}_{Pj,k}$ and the sliding variables $s_{j,k}$ are unknown. The number of unknown variables for $\mathbf{f}_{Pj,k}$ is 2mg, because locally the Z-axis component equals to 0 in the arm local frame. And for $s_{j,k}$ the number is mg. The compatibility equations described above constitute 3mg constraint equations for the m arm tubes and g disks. Thus, we have a nonlinear system of equations to solve in which the 3mg unknown variables are solved iteratively. This process is shown in Fig. 7 and parallels that of [26]. An initial guess of the unknowns will be input to both arm tubes and backbone to solve boundary value problems, however, the arm tubes should be solved first. Then, the orientations of arm tubes $\mathbf{R}_{j,k}$ at each interacting position will be input to the backbone. After solving the shapes of tubes and

backbone, the distance residual will be checked against the compatibility constraints. The stop criterion will be met when the sum of squares of the residual is less than 1mm, otherwise the root finding algorithm will update the solution and solve the aforementioned boundary value problems on tubes and backbone again. The whole solving process will end until convergence criteria met.

The implementation considerations of the introduced model are in two aspects. On one hand, the differential equations and boundary conditions for tubes and backbone can be formulated as several individual boundary value problems (BVPs) to be solved. It is noted that BVPs of tubes should be solved before solving backbone as the latter needs tube orientation $\mathbf{R}_{j,k}$ as inputs. Given the sliding and the interactive forces, one way to find the solutions to the BVPs is by shooting method that iteratively finds the initial curvature and cross section force for all the tubes and the backbone. In this paper, we solve the BVPs using MATLAB's bvp5c command which is based on the three- stage Lobatto Ilia formula. On the other hand, standard root finding algorithms such as Newton's method could be used to solve the nonlinear equations about sliding and interactive point forces. We solve the system of equations by using MATLAB's fsolve command and Levenberg-Marquardt algorithm.

IV. Numerical Evaluation of Workspace

To investigate the workspace that can be reached using the two-arm sheath design, simulations were performed using the parameters given in Table I. This design employs six intermediate disks along the backbone at intervals of 20mm. Two eccentric offsets of the arms from the central backbone are considered, $\|\mathbf{r}_j\| = \{4,8\}$ mm. Configurations were computed for the arm rotation angles, $a_{I,2}$ for 8 uniformly sampled angles in the $[0,2\pi)$; therefore the number of all rotation combinations is 64.

A. Worskspace Boundary

Given that the precurved tubes are of the same stiffness and pre-curvature, we anticipate that the tip of the sheath will sweep out a solid angle that includes the straight configuration, corresponding to tube orientations as shown in Fig. 3. The configurations of maximum curvature will correspond to configurations in which the two tube angles are equal, $a_1 = a_2$. Four such configurations of the 4mm eccentricity case are shown in Fig. 8. The 8mm eccentricity case shows the same workspace boundary. The points in black are depicting the distal end disk positions from the sampled configurations. Notice how the arm channels do not experience any roll or twisting with respect to the sheath as the workspace boundary is traced out.

Another interesting thing to note is that the maximum curvature is constant around the boundary, consider that for the configurations closest to and farthest from the reader occur when the precurved tubes are lie on the neutral axis of bending. In this case, it can be anticipated that the resultant curvature can be calculated by considering the precurved tubes and backbone as parallel springs of equal curvature. The fact that the left and right configurations have the same backbone curvature as the front and back configurations is perhaps a little surprising since neither precurved tubes lies on the neutral axis for these configurations. Thus, the two tubes and the backbone all have different radii of curvature.

Nevertheless, the neutral axis curvature remains constant as the sheath traces out its workspace boundary.

B. Workspace Interior

To reach sheath curvatures between zero and the maximum value, the relative angle between the two tube angles can be varied between 0 and π . The sheath will trace out a circle of constant curvature for any fixed relative angle in this range as the red circle shown in Fig. 8. When keeping one tube angle constant and rotating the other one for 2π , the sheath will trace out a smaller circle as depicted as the green lines. Note that the sheath will experience some twist between zero and the maximum angle of Fig. 9 that will depend on the relative angle of the arm tubes.

C. Sheath Roll or Twisting

The sheath assumes a straight configuration for tube angles such as those of Fig. 3. In the two configurations of Figs. 3(a) and (b), the curvature of the arm tubes lie in the same plane as the central backbone and so the sheath does not twist. For the configuration of Fig. 3(c), however, the precurvature of the arm tubes creates a twisting moment on the central backbone. This is depicted in Fig. 9 which depicts the twisting of the sheath for the set of straight configurations, $a_1 = a_2 + \pi$. As the arm tubes rotate while satisfying this constraint, the twist angle of the tip of the sheath oscillates over an angle range of $|a_0| = a_{0,\text{max}}$. As shown in Fig. 9, the value of $a_{0,\text{max}}$ depends on the eccentric offset of the arms from the central backbone. This result can be anticipated since the eccentricity determines the torsional moment arm on the central backbone.

V. Experimental> Validation

To validate the concept and model, a prototype was constructed as shown in Fig. 10 with parameters given in Table II. To simplify construction, precurved NiTi wires were used in place of tubes to represent the arm channels. The backbone was made from polyimide tubing with spacer disks fabricated by 3D printing with sets of holes at eccentricity distances of 4 and 8mm. The disks themselves were 1mm thick and 18mm in diameter.

An electromagnetic tracking system (3D Guidance trak- STAR, Ascension Co.) was used to record the base and tip positions and orientations for a set of 16 uniformly sampled combinations of wire base angles. Measurements were made for the two eccentricity distances.

To compare these measurements to the model, the relative stiffness of the backbone to the arms was calculated by measuring the deflection on the workspace boundary and comparing it to the precurvature of the wires. It was defined as the ratio of the two nominal bending stiffnesses listed in Table II. Relative stiffness was used together with the other parameters of Table II to simulate the tip coordinates for the measured configurations.

As shown in Fig. 10, the shape of the workspace is as anticipated by the model. We define position and orientation errors between the model and experiment as

$$err_p = \|\mathbf{p}_m - \mathbf{p}_e\|, \quad err_R = \theta (\mathbf{R}_m^{\top} \mathbf{R}_e),$$
 (15)

where the subscripts \cdot_m and \cdot_e denote the position and orientation from model and experimental data, respectively. $\theta(\cdot)$ is to calculate rotation angle from rotation as defined in [27]. The average errors are given in Table III. The maximum errors occur for the straight configurations of the sheath when the precurvatures oppose each other as shown in Fig. 11. This configuration corresponds to the potentially unstable configuration of a concentric tube pair [20]. As shown in the figure, the robot is stable for the 4mm offset distance and unstable for the 8mm offset distance. For the larger offset of Fig. 11(b), friction stabilizes a family of solutions and it was possible to twist the tip of the sheath about its axis to any angle within a range and have it stay at that angle.

VI. Conclusions

The development of miniaturized single-port systems incorporating multiple arms delivered through a steerable sheath could significantly expand the number of and type of minimally invasive procedures that can be performed in fields like neurosurgery. To address this need, we have proposed a steerable sheath technology based on the rotation of eccentrically combined precurved tubes that serve as the working channels for the robotic arms.

While a two-arm sheath actuated using pure rotation was considered here, the work is easily extended to consider rotation plus push/pull actuation as well as more arms. For example, a third "arm" could be used for the imaging system and the three actuation tubes would then match the standard number of push/pull tendons. While the initial results are promising, more work is needed to understand the limits of the approach in comparison to existing methods.

Acknowledgments

This work is supported by the NIH under grant R01NS099207.

References

- [1]. Ren H, Lim CM, Wang J, Liu W, Song S, Li Z, Herbert G, Tse ZTH, and Tan Z, "Computer-assisted transoral surgery with flexible robotics and navigation technologies: a review of recent progress and research challenges," Critical Reviews in Biomedical Engineering, vol. 41, no. 4–5, 2013.
- [2]. Song S, Zhang C, Wang J, Meng MQ-H, and Ren H, "Realtime shape estimation of curvilinear flexible surgical robots: Methods, experiments and analysis," International Journal of Robotics and Automation, vol. 33, no. 5, 2018.
- [3]. Warf BC, "Endoscopic third ventriculostomy and choroid plexus cauterization for pediatric hydrocephalus," Clinical neurosurgery, vol. 54, p. 78, 2007. [PubMed: 18504900]
- [4]. Warf BC, "Comparison of endoscopic third ventriculostomy alone and combined with choroid plexus cauterization in infants younger than 1 year of age: a prospective study in 550 african children," Journal of Neurosurgery: Pediatrics, vol. 103, no. 6, pp. 475–481, 2005. [PubMed: 16383244]
- [5]. Warf BC, "Hydrocephalus in uganda: the predominance of infectious origin and primary management with endoscopic third ventriculostomy," Journal of Neurosurgery: Pediatrics, vol. 102, no. 1, pp. 1–15, 2005.

[6]. Warf BC and Campbell JW, "Combined endoscopic third ventriculostomy and choroid plexus cauterization as primary treatment of hydrocephalus for infants with myelomeningocele: long-term results of a prospective intent-to-treat study in 115 east african infants," Journal of Neurosurgery: Pediatrics, vol. 2, no. 5, pp. 310–316, 2008. [PubMed: 18976099]

- [7]. Cappabianca P, Cinalli G, Gangemi M, Brunori A, Cavallo LM, de Divitiis E, Decq P, Delitala A, Di Rocco F, Frazee J, et al., "Application of neuroendoscopy to intraventricular lesions," Neurosurgery, vol. 62, no. suppl_2, pp. SHC575–SHC598, 2008.
- [8]. Apuzzo ML, Dobkin WR, Zee C-S, Chan JC, Giannotta SL, and Weiss MH, "Surgical considerations in treatment of intraventricular cysticercosis: an analysis of 45 cases," Journal of neurosurgery, vol. 60, no. 2, pp. 400–407, 1984. [PubMed: 6607328]
- [9]. Anor T, Madsen JR, and Dupont P, "Algorithms for design of continuum robots using the concentric tubes approach: A neurosurgical example," in Robotics and Automation (ICRA), 2011 IEEE International Conference on IEEE, 2011, pp. 667–673.
- [10]. Gaab MR and Schroeder HW, "Neuroendoscopic approach to intraventricular lesions," Journal of neurosurgery, vol. 88, no. 3, pp. 496–505, 1998. [PubMed: 9488304]
- [11]. Oka K, Yamamoto M, Nagasaka S, and Tomonaga M, "Endoneu- rosurgical treatment for hydrocephalus caused by intraventricular tumors," Child's Nervous System, vol. 10, no. 3, pp. 162–166, 1994.
- [12]. Bahuleyan B, Manjila S, Robinson S, and Cohen AR, "Minimally invasive endoscopic transventricular hemispherotomy for medically intractable epilepsy: a new approach and cadaveric demonstration," Journal of Neurosurgery: Pediatrics, vol. 6, no. 6, pp. 536–540, 2010. [PubMed: 21121727]
- [13]. Souweidane MM, "Endoscopic surgery for intraventricular brain tumors in patients without hydrocephalus," Operative Neurosurgery, vol. 57, no. suppl_4, pp. ONS–312, 2005.
- [14]. Badie B, Brooks N, and Souweidane MM, "Endoscopic and minimally invasive microsurgical approaches for treating brain tumor patients," Journal of neuro-oncology, vol. 69, no. 1–3, pp. 209–219, 2004. [PubMed: 15527092]
- [15]. Yeung BPM and Gourlay T, "A technical review of flexible endoscopic multitasking platforms," International journal of surgery, vol. 10, no. 7, pp. 345–354, 2012. [PubMed: 22641123]
- [16]. Camarillo DB, Carlson CR, and Salisbury JK, "Configuration Tracking for Continuum Manipulators With Coupled Tendon Drive," IEEE Transactions on Robotics, vol. 25, no. 4, pp. 798–808, 8 2009.
- [17]. Bajo A, Pickens RB, Herrell SD, and Simaan N, "Constrained motion control of multisegment continuum robots for transurethral bladder resection and surveillance," in 2013 IEEE International Conference on Robotics and Automation, 5 2013, pp. 5837–5842.
- [18]. Goldman RE, Bajo A, MacLachlan LS, Pickens R, Herrell SD, and Simaan N, "Design and Performance Evaluation of a Minimally Invasive Telerobotic Platform for Transurethral Surveillance and Intervention," IEEE Transactions on Biomedical Engineering, vol. 60, no. 4, pp. 918–925, 4 2013. [PubMed: 23144027]
- [19]. Sarli N, Del Giudice G, De S, Dietrich MS, Herrell SD, and Simaan N, "Preliminary porcine in vivo evaluation of a telerobotic system for transurethral bladder tumor resection & surveillance," Journal of Endourology, pp. -, 3 2018 [Online]. Available: http://www.liebertpub.com/doi/10.1089/end.2018.0119
- [20]. Dupont PE, Lock J, Itkowitz B, and Butler E, "Design and Control of Concentric-Tube Robots," IEEE Transactions on Robotics, vol. 26, no. 2, pp. 209–225, 2010. [PubMed: 21258648]
- [21]. Yu H, Wu L, Wu K, and Ren H, "Development of a multi-channel concentric tube robotic system with active vision for transnasal nasopharyngeal carcinoma procedures," IEEE Robotics and Automation Letters, vol. 1, no. 2, pp. 1172–1178, 7 2016.
- [22]. Sears P and Dupont P, "A steerable needle technology using curved concentric tubes," in Intelligent Robots and Systems, 2006 IEEE/RSJ International Conference on IEEE, 2006, pp. 2850–2856.
- [23]. Xu K and Simaan N, "Analytic formulation for kinematics, statics, and shape restoration of multibackbone continuum robots via elliptic integrals," Journal of Mechanisms and Robotics, vol. 2, no. 1, p. 011006, 2010.

[24]. Black CB, Till J, and Rucker DC, "Parallel continuum robots: Modeling, analysis, and actuation-based force sensing," IEEE Transactions on Robotics, vol. 34, no. 1, pp. 29–47, 2018.

- [25]. Murray RM, Li Z, and Sastry SS, A mathematical introduction to robotic manipulation. Boca Raton: CRC Press, 1994.
- [26]. Orekhov AL, Aloi VA, and Rucker DC, "Modeling parallel continuum robots with general intermediate constraints," in 2017 IEEE International Conference on Robotics and Automation (ICRA), 5 2017, pp. 6142–6149.
- [27]. Wu L, Wang J, Qi L, Wu K, Ren H, and Meng MQ-H, "Simultaneous hand-eye, tool-flange, and robot-robot calibration for comanipulation by solving the AXB= YCZ problem," IEEE TRansactions on robotics, vol. 32, no. 2, pp. 413–28, 2016.

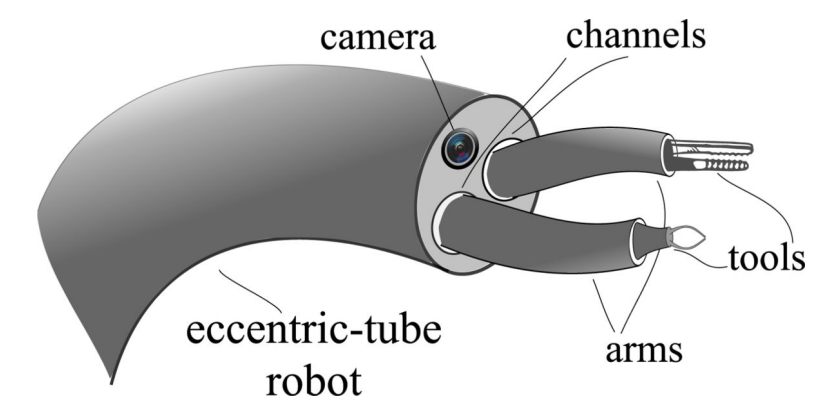


Fig. 1.

Conceptual design of a 2-channel eccentric-tube robot with two continuum arms delivered through the channels. The channels are constructed from pre-curved tubes and are designed to act as both delivery channels and actuating elements. Tube rotation at proximal end controls the shape of the sheath.

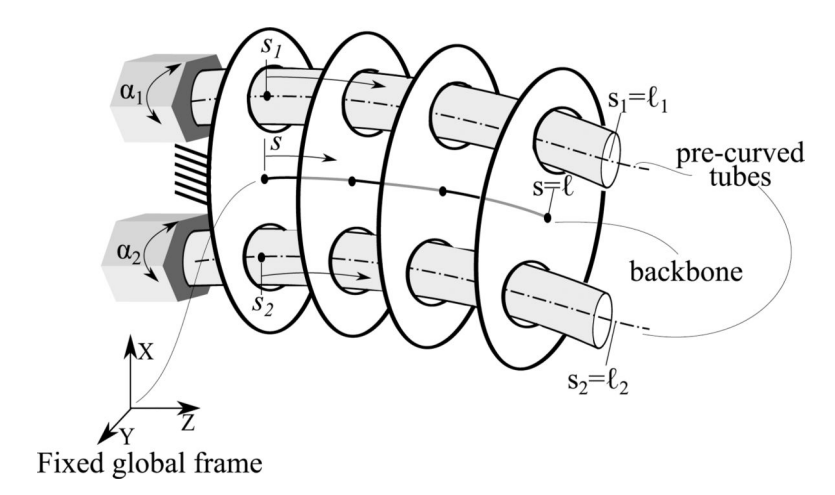


Fig. 2. Schematic of steerable sheath for two arms. The arm working channels are lined with precurved tubes that are rotated through the angles $\{\alpha_1, \alpha_2\}$ to bend and straighten the sheath. A central backbone is used maintain disk spacing along the axis of the sheath.

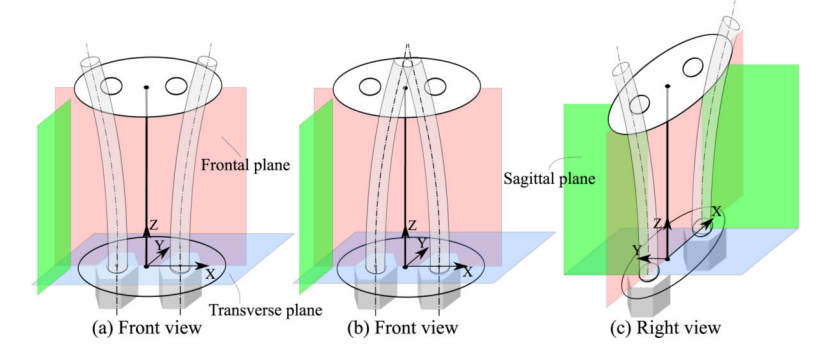


Fig. 3. Arm tube configurations to produce a straight sheath. Unconstrained tube shapes are depicted in order to make configurations clear. (a) Precurvatures are coplanar and facing away from each other. (b) Coplanar precurvatures are facing each other. (c) Precurvatures oppose each other, but are not coplanar.

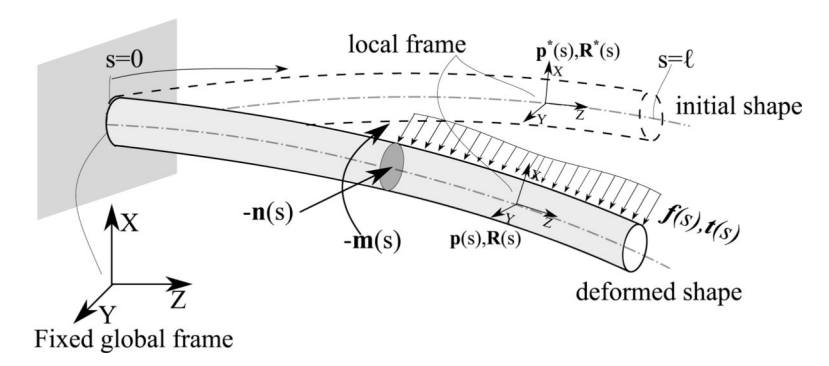


Fig. 4.
Single pre-curved tube under an arbitrary external distributed force and moment load.
Bishop convention is used to define global and local frames, i.e., Z-axis is aligned with the tangent direction of the rod. For the rod without external load, the local frame is defined as if it slides from the proximal end to the distal end without Z-axis rotation.

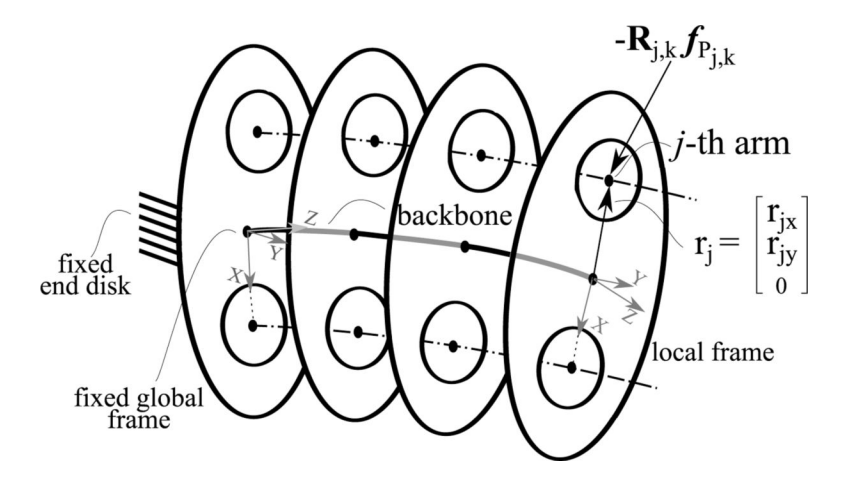


Fig. 5. Backbone can be regarded as a single cantilevered rod that subjects to external point force – $\mathbf{f}_{p,j,k}$ from the *j*-th arm *k*-th disk.

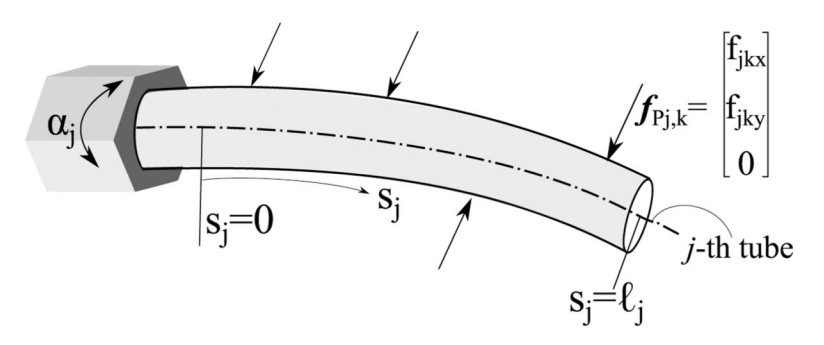


Fig. 6. The *j*-th tube from ETR can be regarded as a single cantilevered rod that subjects to external point forces $\mathbf{f}_{p,j,k}$ from k-th disk.

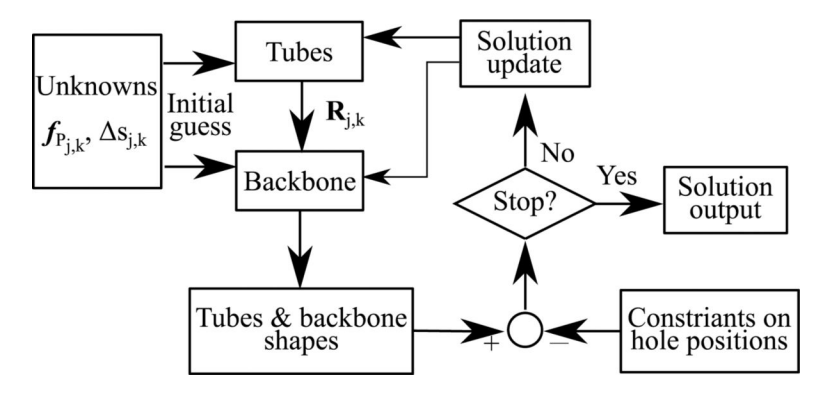


Fig. 7. Block diagram of the non-linear system of compatibility constraints.

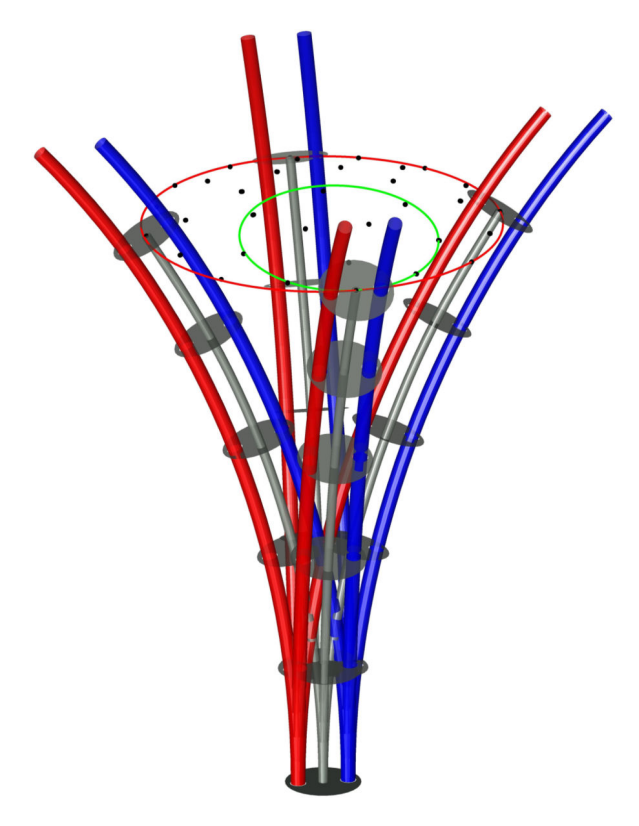


Fig. 8. Workspace of two-arm sheath of 4mm eccentricity. Depicted configurations lie on workspace boundary. Red circle traces tip of central backbone on workspace boundary while green circle traces motion boundary when keeping one tube angle constant and rotating the other one for 2π .

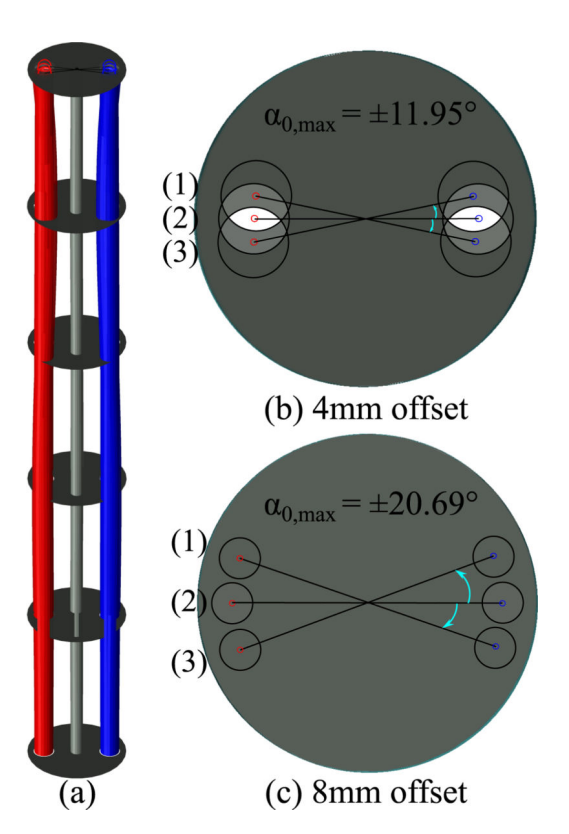


Fig. 9.Twisting of sheath in straight configurations. (a) Sheath. (b) Sheath tip twisting for 4mm eccentricity. (c) Sheath tip twisting for 8mm eccentricity.

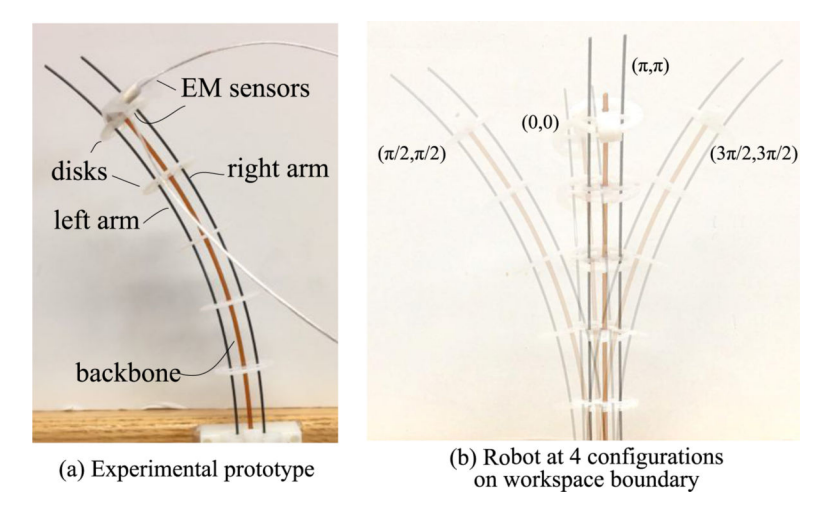
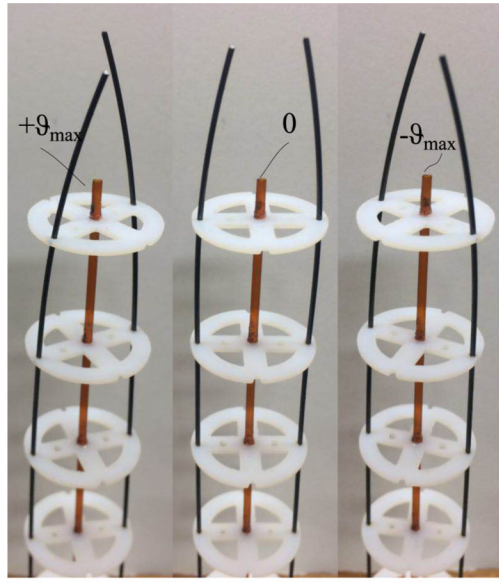


Fig. 10. Prototype of two-arm sheath. Precurved wires are used in place of arm tubes to simply construction. Depicted eccentricity (distance between centerlines of arms and central backbone) is 4mm. (a) Electromagnetic (EM) sensors are mounted on the distal disk to measure position and orientation, (b) Robot at 4 configurations on workspace boundary.





(a) 4mm offset

(b) 8mm offset

Straight configuration of Fig. 3(b). (a) Solution for 4mm eccentricity is stable. (b) A family of marginally stable solutions involving twisting of the sheath is observed for an 8mm eccentricity.

TABLE I

Parameters of a 2-channel balanced-pair ETR for the simulations.

	Tube 1 & 2	Backbone
Young's modulus (GPa)	75	75
Poisson's ratio	0.33	0.42
Radius of curvature (mm)	170.30	_∞
Curve length (mm)	140	100
Outer diameter (mm)	2.50	1.50
Inner diameter (mm)	2.20	-

Table II

Parameters of the ETR prototype for experiments.

	Tube 1 & 2	Backbone
Nominal K_b (N·m)	1.40×10^{-3}	4.99×10^{-4}
Nominal $K_t(N \cdot m)$	1.0×10^{-3}	3.51×10^{-4}
Radius of curvature (mm)	230.72	œ
Curve length (mm)	120	100
Outer diameter (mm)	0.76	1.25
Inner diameter (mm)	-	1.04

Table III

Average errors between simulations and experiments.

Eccentricity	err_p (mean \pm std)	err_R (mean \pm std)
4mm	6.77 ±2.81mm	10.29 ±3.86°
8mm	10.91 ±4.32mm	13.11 ±4.83°